Journal of Energy Chemistry 55 (2021) 211–218

Contents lists available at ScienceDirect

Journal of Energy Chemistry

journal homepage: www.elsevier.com/locate/jechem

http://www.journals.elsevier.com/journal-of-energy-chemistry/

A crosslinked polymer as dopant-free hole-transport material for efficient n-i-p type perovskite solar cells

Linqin Wang [a,1], Fuguo Zhang [a,1], Tianqi Liu [a], Wei Zhang [b], Yuanyuan Li [c], Bin Cai [d], Lanlan He [b], Yu Guo [b], Xichuan Yang [d], Bo Xu [a,*], James M. Gardner [b], Lars Kloo [b], Licheng Sun [a,d,*]

[a] Organic Chemistry, Centre of Molecular Devices, Department of Chemistry, KTH Royal Institute of Technology, SE-10044 Stockholm, Sweden
[b] Applied Physical Chemistry, Centre of Molecular Devices, Department of Chemistry, KTH Royal Institute of Technology, SE-10044 Stockholm, Sweden
[c] Wallenberg Wood Science Centre, Department of Fibre and Polymer Technology, KTH Royal Institute of Technology, SE-10044 Stockholm, Sweden
[d] State Key Laboratory of Fine Chemicals, Institute of Artificial Photosynthesis, DUT-KTH Joint Education and Research Centre on Molecular Devices, Dalian University of Technology, Dalian 116024, Liaoning, China

ARTICLE INFO

Article history:
Received 12 May 2020
Revised 23 June 2020
Accepted 29 June 2020
Available online 9 July 2020

Keywords:
Perovskite solar cell
Hole-transport material
Dopant-free
Crosslinked polymer
Spiro[fluorene-9,9′-xanthene] (SFX)

ABSTRACT

A new crosslinked polymer, called **P65**, with appropriate photo-electrochemical, opto-electronic, and thermal properties, has been designed and synthesized as an efficient, dopant-free, hole-transport material (HTM) for n-i-p type planar perovskite solar cells (PSCs). **P65** is obtained from a low-cost and easily synthesized spiro[fluorene-9,9′-xanthene]-3′,6′-diol (SFX-OH)-based monomer **X65** through a free-radical polymerization reaction. The combination of a three-dimensional (3D) SFX core unit, hole-transport methoxydiphenylamine group, and crosslinked polyvinyl network provides **P65** with good solubility and excellent film-forming properties. By employing **P65** as a dopant-free hole-transport layer in conventional n-i-p type PSCs, a power conversion efficiency (PCE) of up to 17.7% is achieved. To the best of our knowledge, this is the first time a 3D, crosslinked, polymeric dopant-free HTM has been reported for use in conventional n-i-p type PSCs. This study provides a new strategy for the future development of a 3D crosslinked polymeric dopant-free HTM with a simple synthetic route and low-cost for commercial, large-scale applications in future PSCs.

1. Introduction

Organic-inorganic hybrid perovskite solar cells (PSCs) have been a promising candidate for third-generation photovoltaics (PVs), and the power conversion efficiency (PCE) has surged to 25.2% as of 2019 [1–3]. Meanwhile, studies on PSCs, including fabrication techniques, device architectures, functional components, and new materials, have been systematically and intensively investigated [4–8]. The hole-transport materials (HTMs) play a pivotal role in extracting and transporting holes as well as restraining the charge recombination at the interfaces between the perovskite layer and the hole transport layer [9,10]. Moreover, in conventional n-i-p type PSCs, HTMs act as a protective layer to prevent moisture in the air from permeating and degrading the perovskite materials. This improves the stability and device performance of the PSCs [11,12]. However, owing to the intrinsically low hole mobility and conductivity, even for the benchmark HTM, N^2,N^2,$N^{2'}$,$N^{2'}$,N^7,N^7,$N^{7'}$,$N^{7'}$-octakis(4-methoxyphenyl)-9,9′-spirobi[9H-fluorene]-2,2′,7,7′-tetramine (Spiro-OMeTAD), the hygroscopic additives, such as bis(trifluoromethane)sulfonimide lithium salt (LiTFSI), and tert-butylpyridine (*t*-BP), are typically required to improve the charge transport ability to guarantee a significantly better solar cell performance [13–15]. Nevertheless, the application of dopants will inevitably incur offside-effects, for instance, an acceleration of the degradation of the perovskite layer and a poor stability of the solar cells [16,17]. In this regard, a search for potential dopant-free HTM candidates is significant for the practical application of PSCs.

Several novel, dopant-free HTMs aiming to improve the stability of PSCs and achieve excellent PCEs have been designed and synthesized [18–23]. For example, varieties of small organic molecules with different core units, including triphenylamine (TPA) [24,25], tetrathiafulvalene (TTF) [26], tetrathienylethene (TTE) [27], dithieno[3,2-b:2′,3′-d]pyrrole (DTP) [28], and triazatruxene [29],

* Corresponding authors at: Organic Chemistry, Centre of Molecular Devices, Department of Chemistry, KTH Royal Institute of Technology, SE-10044 Stockholm, Sweden (L. Sun).
E-mail addresses: box@kth.se (B. Xu), lichengs@kth.se (L. Sun).
[1] These authors contributed equally to this work.

https://doi.org/10.1016/j.jechem.2020.06.062
2095-4956/

have been extensively investigated. In addition, some metal complexes and inorganic p-type semiconductors have also been considered as dopant-free HTMs, such as copper(II) phthalocyanines (CuPcs) [30], and CuSCN [31]. Such systems typically show a good intrinsic hole mobility, conductivity, and low cost.

In addition to small molecules [32,33], polymer-based HTMs have attracted considerable attention owing to their good thermal stability, tunable functionality, mechanical flexibility, and good film-forming ability, among other benefits [34,35]. One of the common strategies in the design of dopant-free HTMs is the use of donor–acceptor (D-A) conjugation building blocks, which are easy to apply owing to their tunable electrical and optical properties and improved charge-transport characteristics [36–38]. For example, Park et al. combined two polymers, P-OR and P-R, to form a random copolymer RCP as an HTM layer and yielded a PSC PCE of 17.3% [39]. Both polymers displayed a coplanar donor with π-π stacking and a strong electron acceptor, generating a good charge mobility and a suitable HOMO energy level. Undoubtedly, D-A-type, dopant-free HTMs have shown significant potential for use in solar cell devices [40]. Nevertheless, requirements involving noble-metal catalysts and expensive raw materials, complicated synthesis routes and purification procedures, and an intrinsic colored and unsatisfactory solubility limit their further application.

Another type of attractive dopant-free, polymeric HTM is a non-π-conjugation polymer formed through a free-radical polymerization with a double bond, which has been widely used in electrochromic devices (ECDs) [41], organic light-emitting diodes (OLEDs) [42], and organic photovoltaics (OPVs) [43]. Linear structured polymers with different side chains have also been developed [44]. Huang et al. reported a non-conjugated carbazole-based polymer (PVCz-OmeDAD) as a dopant-free HTM for n-i-p-type PSCs, achieving an efficiency of 16.09% [45]. Compared to linear polymers, crosslinked polymers with three-dimensional (3D) network structures provide a higher density of the charge-transport channels, a good solvent/thermal resistance, and mechanical durability [46–48]. Shao et al. employed four diphenylamine derivatives with a fluorene core as HTMs in inverted p-i-n planar PSCs using *in-situ* annealing, and achieved a PCE of 18.7% [49]. Some other crosslinked 3D HTMs, e.g., N^4,$N^{4'}$-Di(naphthalen-1-yl)-N^4,$N^{4'}$-bis(4-vinylphenyl)biphenyl-4,4′-diamine, termed VNPB, have been applied in semi-transparent PSCs along with an extra deep-work-function transition metal oxide (typically MoO_3) as an interface doping layer [50,51]. However, little attention has been focused on the development of 3D crosslinked polymers as dopant-free HTMs for use in n-i-p-type PSCs.

Herein, we present a novel spiro[fluorene-9,9′-xanthene]-3′,6′-diol (SFX-OH)-based, crosslinked polymer, **P65**, obtained through a mild free-radical polymerization as a dopant-free HTM for n-i-p-type PSCs (Fig. 1). This polymer is characterized by suitable energy levels, adequate charge-transport properties, and good thermal stability and hydrophobicity. An impressive PCE of 17.7% was achieved in PSCs using the newly designed polymer-**P65** as an HTM. To the best of our knowledge, this is the first time a 3D, crosslinked-polymeric, dopant-free HTM has been used in a conventional n-i-p-type PSC.

2. Experimental

2.1. Materials

All solvents and chemicals used in this study are commercially available and were applied as received unless stated otherwise. The experimental details regarding the synthesis and characterization, as well as the DFT calculations, are provided in the Supporting Information.

2.2. Device fabrication

Perovskite solar cells: A fluorine-doped tin oxide (FTO) substrate (TEC 15, Hartford Glass Co.) was patterned using a hydrogen-evolution etching method (zinc powder and a 2 M HCl solution). Pre-patterned FTO was cleaned in soapy water, deionized water, acetone, and ethanol with sonication, and all substrates were then UV-ozone cleaned for 30 min subsequently before further use, followed by deposition with a thin compact TiO_2 layer through spray pyrolysis using 0.2 M $Ti(acac)_2OiPr_2$ in an isopropanol solution at 450 °C. The sprayed film was annealed at 450 °C for 30 min. Tin oxide was used as an electron transport material. The 15% tin oxide colloid precursor was diluted to 2.67% using deionized water. The solution was spun onto the FTO glass/compact TiO_2 substrate surface at 3000 rpm for 30 s, and then baked on a hotplate in an ambient atmosphere at 120 °C for 20 min. The as-prepared substrates were further cleaned using an UV-ozone cleaner for 20 min before use. The perovskite film was subsequently deposited using the aforementioned spin-coating methods. A hole-transport layer (HTL) was then spin-coated onto the perovskite films. The conventional doped-Spiro-OMeTAD was spun at 4000 rpm for 30 s with an HTL solution consisting of 85.8 mg of Spiro-OMeTAD, 19.3 μL Li-TFSI stock solution (520 mg Li-TFSI in 1 mL acetonitrile), 30 μL *t*-BP, 10.52 μL FK209 (tris(2-(1H-pyrazol-1-yl)-4-tert-butylpyridine)cobalt(III) tri[hexafluorophosphate]) stock solution (300 mg FK209 in 1 mL of acetonitrile), and 1 mL chlorobenzene solvent. For **P65**, different concentrations (5, 10, and 15 mg/mL) of HTM without dopants were applied. Finally, an 80-nm layer of gold was deposited through thermal evaporation using a shadow mask to pattern the electrodes.

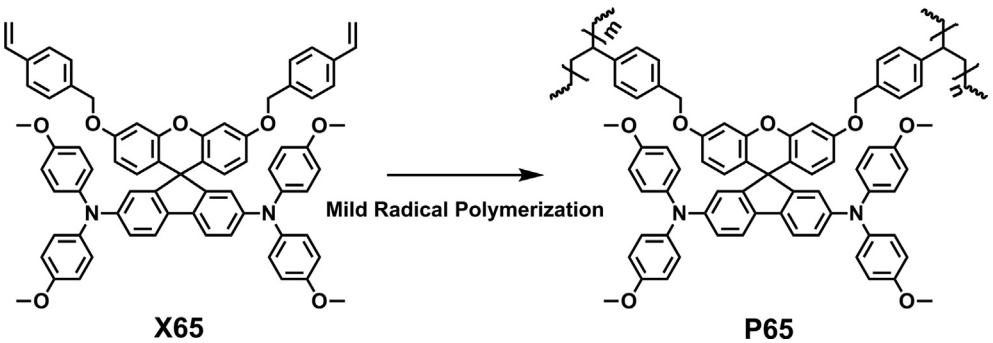

Fig. 1. Chemical structures of HTM **X65** and **P65**.

3. Results and discussion

3.1. Materials synthesis

The synthetic route of the HTM monomer (**X65**) and polymer (**P65**) is shown in Scheme S1. The design of the HTMs is based on the spiro[fluorene-9,9′-xanthene] (SFX) unit core, which contains a central tetrahedral sp^3 carbon atom and two perpendicular π systems, i.e., xanthene and fluorene [52,53]. This 3D-structural skeleton has been demonstrated to decrease the charge recombination process and increase the electronic coupling in solar cell devices [54,55]. In addition, the flexible vinyl groups not only act as reactive sites for radical polymerization, they can also be beneficial for increasing the solubility of the material [56].

The monomer **X65** was synthesized through an extremely simple three-step procedure with a high yield. The synthesis was initiated using the construction of a 2,7-dibromospiro[fluorene-9,9′-xanthene]-3′,6′-diol (SFX-OH) core through a cyclization reaction, followed by a substitution reaction to anchor the functional group 4-vinylbenzyl; finally, the product **X65** was completed through a palladium-catalyzed Buchwald-Hartwig cross-coupling reaction. The polymer HTM **P65** was obtained using a free-radical polymerization of the corresponding monomers with 2,2′-azobis(2-methyl propionitrile) (AIBN) as an initiator, and the product was purified with different solvents (more detailed information is provided in the Supporting Information) through a Soxhlet extraction according to published procedures [42]. Both the HTM **X65** and **P65** show good solubility in common organic solvents, such as chloroform, toluene, tetrahydrofuran, and chlorobenzene. The composition and chemical structures of all intermediates were confirmed using ^{1}H and ^{13}C NMR spectroscopy and matrix-assisted laser desorption ionization time-of-flight mass spectrometry (MALDI-TOF) (Figs. S1–S6). The size and molecular weight of the polymer were estimated using size exclusion chromatography (SEC) (see the Supporting Information), to render a number-average molecular weight (M_n) of 153,057 g/mol, a corresponding weight-average molecular weight (M_w) of 442,495 g/mol, and a relatively low polydispersity (PDI = M_w/M_n) of 2.89. DFT calculations were conducted to understand the crosslinked structure of **P65**, as shown in Fig. S14. In addition, a brief cost estimation for the synthesis of 1 g of **P65** is given in Scheme S2 and Table S5, and roughly comprises 20% that of Spiro-OMeTAD, as shown in Scheme S3 and Table S6. For low-cost raw materials, a simple synthesis route and a high overall yield show a promising scale-up of **P65** for commercial application.

3.2. Optical and electrochemical properties

The normalized UV–visible absorption and photoluminescence (PL) spectra, recorded in a 10^{-5} M dichloromethane solution, are shown in Fig. 2(a). No apparent influence of the polymerization process on the absorption and PL properties of the two compounds was shown. Both **X65** and **P65** show a broad shoulder peak at approximately 375–386 nm and no distinct light absorption within visible range. In the PL spectra, **X65** and **P65** show similar emissions at 427 and 426 nm, respectively. The optical band gaps of the two HTMs are 3.04 and 3.03 eV, respectively, which are close to that of Spiro-OMeTAD (3.05 eV), as estimated from the intersection of the normalized absorption and emission spectra.

The oxidation potentials (E_{OX}) and highest occupied molecular orbital (HOMO) energy levels of **X65** and **P65** were obtained from cyclic voltammetry (CV) (Fig. S7) and differential pulsed voltammetry (DPV) (Fig. 2b), as recorded from a 10^{-4} M dichloromethane solution. The corresponding data are summarized in Table 1. The small molecular substance **X65** shows a similar HOMO energy level as Spiro-OMeTAD (-5.09 and −5.08 eV, respectively), whereas **P65** displays a marginally deeper HOMO energy level of −5.12 eV. Despite the matched energy alignment with respect to the perovskite and electrode materials, the deeper HOMO energy level of **P65** probably decreases the potential voltage loss, and thus a slightly higher open-circuit voltage in the corresponding solar cell devices can be anticipated. The lowest unoccupied molecular orbital (LUMO) energy levels of the HTMs were calculated using the optical band gap and HOMO energy levels. Both HTMs show suitable LUMO energy levels (-2.05 eV for **X65** and −2.09 eV for **P65**) with respect to the conduction band (CB) energy of the perovskite layer. This may suppress the charge-transfer losses between the perovskite layer and the Au back electrode. The energy level diagrams are shown in Fig. 2(c).

3.3. Thermal properties

The thermal properties of the HTMs **X65** and **P65** and Spiro-OMeTAD were investigated through a thermogravimetric analysis (TGA) and differential scanning calorimetry (DSC) (Fig. 2d, 2e, 2f, and Fig. S8). The TGA traces in Fig. 2(d) show an outstanding thermal stability for both HTMs, and the decomposition temperatures (T_d) of **X65** and **P65**, defined as the 2% weight loss temperature, are 317 °C and 381 °C, respectively. It is also worth noting that **X65** from ~200 °C displays a weight loss, which could be attributed to an exothermic process caused by a heat-induced self-polymerization. Similar phenomena can be observed in the DSC results shown in Fig. 2(e). The DSC analysis reveals a stable amorphous state of the HTM **P65** based on a higher glass transition temperature (T_g) of 266 °C (Fig. 2f) than that of its corresponding monomeric material **X65** (T_g of 90 °C before polymerization, thermally crosslinked at 199 °C, as indicated in Fig. 2e) and Spiro-OMeTAD (T_g of 120 °C, as shown in Fig. S8), most likely owing to the higher molecular weight of its building blocks [56].

3.4. Charge-carrier mobility

The *J-V* curve models of the conductivity and hole mobility for the two HTMs **X65** and **P65** are shown in Fig. 3(a) and 3(b), respectively, whereas the corresponding extracted data are given in Table S1. Both investigations were executed for the dopant-free materials, and the concentrations of the HTM precursor solutions were the same as those used for the solar cell device manufacturing. Clearly, **P65** demonstrates a higher hole mobility, i.e., 4.30×10^{-5} cm^2/(V·s), than that of **X65** at 2.77×10^{-5} cm^2/(V·s), which may be attributed to a closer stacking interaction between the monomer fragments after polymerization (Fig. S11). In addition, a polymerized, extended, and conjugated **P65** system requires fewer hopping steps in the conduction channels than the monomeric **X65**. It should also be noted that **P65** exhibits an improved conductivity of 1.20×10^{-6} S/cm as compared to that of **X65** (8.80×10^{-7} S/cm). One further possible reason for the slight difference between the two HTMs could be the excellent film-forming properties of **P65**. The polymeric 3D-network can also be beneficial for an efficient charge transport [57,58].

To probe the charge transfer properties at the interfaces between the perovskite and HTM layers, steady-state photoluminescence (PL) and time-resolved photoluminescence decay (TR-PL) were conducted (Fig. 3c and 3d). As shown in Fig. 3(c), both non-doped **X65**- and **P65**-based films efficiently quench the PL emission of the perovskite layer, suggesting a good hole-extraction capability. Among these films, the **P65**-based film displayed a more efficient PL quenching, indicating a better hole-extraction capability as compared to those of **X65** and Spiro-OMeTAD. These results are further supported by TR-PL traces, as shown in Fig. 3(d). After capping the perovskite layer with

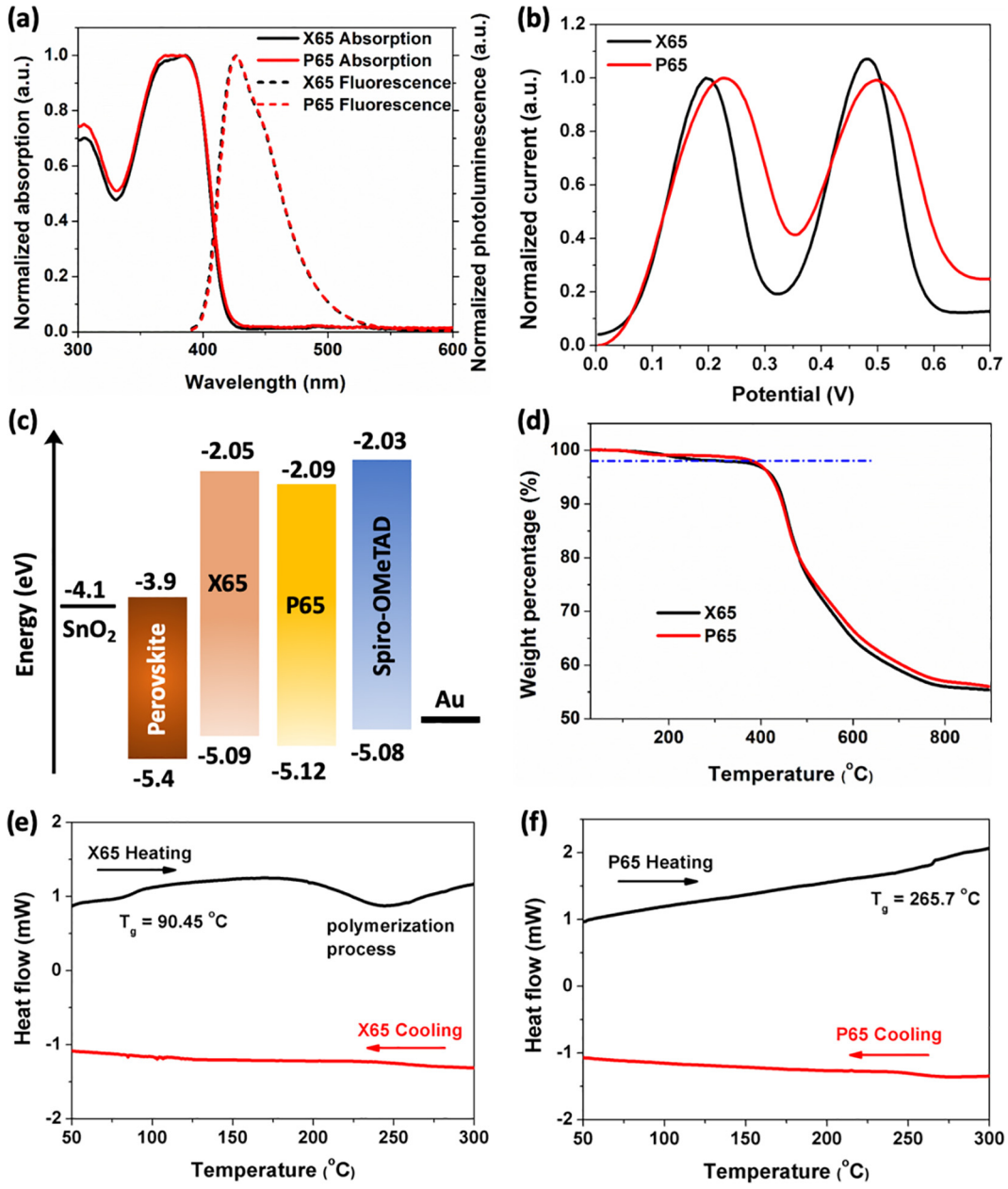

Fig. 2. (a) Normalized UV–visible light absorption and photoluminescence spectra, (b) differential pulsed voltammograms (DPVs) of **X65** and **P65** in dichloromethane, (c) energy level diagram, and (d) thermogravimetric analysis (TGA) traces and differential scanning calorimetry (DSC) scans of **X65** (e) and **P65** (f), respectively.

Table 1
Summary of optical and electrochemical properties of **X65**, **P65**, and Spiro-OMeTAD.

HTMs	λ_{abs} (nm)		λ_{em} (nm)	E_{OX}[a] (V)	$E_{0\text{-}0}$[b] (eV)	HOMO[c] (eV)	LUMO[d] (eV)
X65	295	386	427	0.62	3.04	−5.09	−2.05
P65	295	375	426	0.65	3.03	−5.12	−2.09
Spiro-OMeTAD	306	386	422	0.62	3.05	−5.08	−2.03

[a] 0.1 M of tetrabutylammoniun hexafluorophosphate (n-Bu_4NPF_6) in dichloromethane as an electrolyte, Ag/0.01 M $AgNO_3$ electrode (acetonitrile as a solvent) as a reference electrode, a glassy carbon disk (3-mm diameter) as the working electrode, and a platinum wire as the counter electrode. Scan rate = 100 mV/s. All redox potentials were calibrated versus the normal hydrogen electrode (NHE) by the addition of ferrocene. The conversion factor $E_{(Fc/Fc+)}$ = 630 mV versus NHE was used. $E^{Fc}_{1/2}$ = 0.20 V.
[b] Estimated from the intersection of the normalized absorption and emission spectra.
[c] HOMO = −5.1 eV − ($E_{1/2} - E^{Fc}_{1/2}$).
[d] LUMO = HOMO + $E_{0\text{-}0}$.

dopant-free **P65** as a hole-transport layer, the perovskite film exhibits the strongest quenching effect along with the shortest lifetime (Table S2), thus minimizing the recombination losses within the bulk. This could contribute to the higher V_{OC} observed in solar cell devices, suggesting an effective hole transfer at the perovskite/HTM interface.

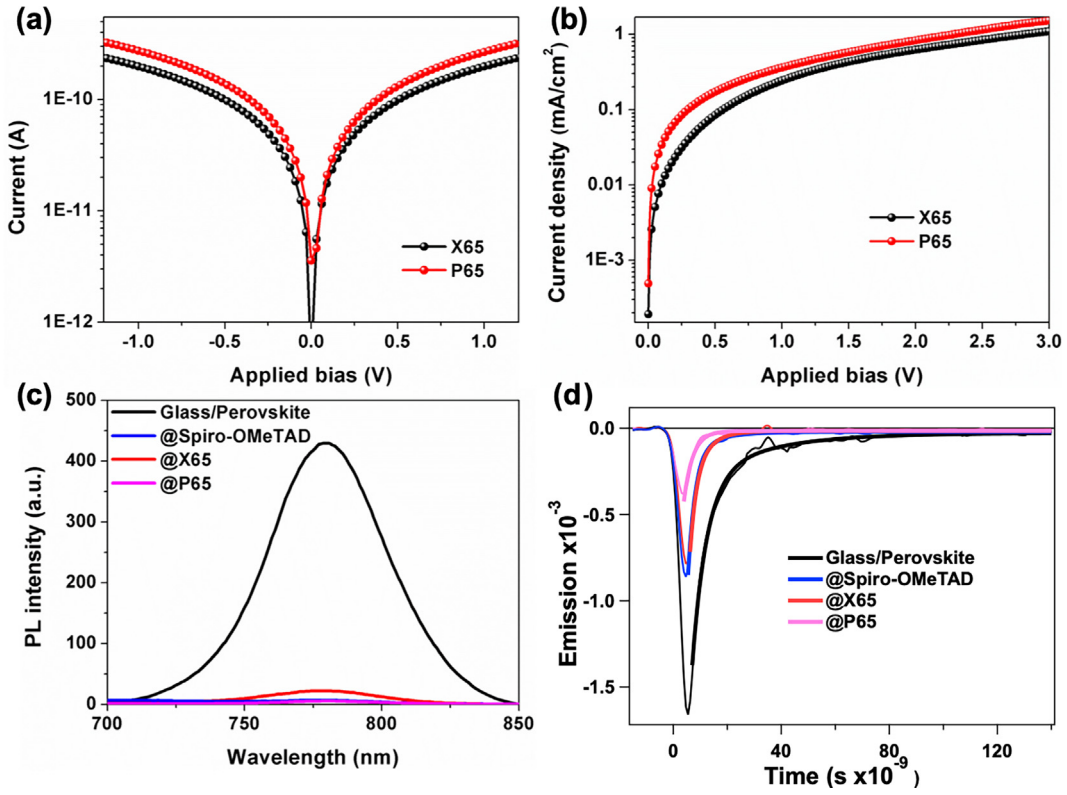

Fig. 3. (a) Conductivity and (b) hole mobility of **X65** and **P65** films (without dopants), respectively, (c) steady-state photoluminescence spectra, and (d) time-resolved photoluminescence kinetic traces at 785 nm along with exponential decay models for a naked perovskite film and for perovskite films capped by the different HTMs.

3.5. Photovoltaic performance of devices

To evaluate the device performance of the synthesized **X65** and **P65**, we fabricated PSCs by employing them as HTMs without any additives. The device architecture was as follows: FTO/compact TiO_2/SnO_2/$MAPbI_3$/HTM/Au [59], which is clearly illustrated by the cross-sectional SEM image shown in Fig. 4(d). All details regarding the fabrication procedure and characterization can be found in the Supporting Information.

Fig. 4(e) shows the photocurrent density versus voltage (*J–V* characteristics) with synthesized small molecular HTM **X65**, polymeric **P65**, and the well-known Spiro-OMeTAD, respectively, when implemented as dopant-free solar cell devices. The corresponding photovoltaic parameters determined from the *J–V* data are analyzed in Table 2. Unexpectedly, the **X65**-based PSC shows a low efficiency of 8.42%. The low photovoltaic performance can be linked to the low conductivity and hole mobility of the material, rendering a higher interface recombination loss. Moreover, in the SEM images of the perovskite layer covered by **X65**, as shown in Fig. 4(b), pinholes can be identified in the film, indicating a poor film-forming ability and further contributing to the reduced solar cell performance. Under the same conditions, the PSC based on the dopant-free **P65** provides an efficiency of 17.7% (reverse scan), whereas the reference of the dopant-free Spiro-OMeTAD-based PSC offers a PCE of 10.6%. The highest open-circuit voltage (V_{OC}) of a **P65**-based device obtained (1.09 V) can probably be ascribed to a combination of a more negative HOMO energy level and less recombination loss compared to devices containing **X65** and Spiro-OMeTAD. The remarkable fill factor (*FF*) recorded for devices based on **P65** (75%) (Table 2) contributes significantly to the device performance (Fig. 4c and 4d). The reduced hysteresis behavior achieved by a dopant-free **P65**-based device can be attributed to the efficient hole extraction and enhanced charge transport between the perovskite layer and the HTM layer [60,61]. The incident photon-to-current-conversion efficiency (IPCE) spectra of **P65**-based PSC devices are shown in Fig. 4(f) and illustrate a wide photoelectric response with respect to the solar spectrum ranging from 400 to 750 nm with a maximum IPCE of greater than 75%. The corresponding integrated short-circuit current density (J_{SC}) calculated from the IPCE spectra is 20.1 mA/cm, which is in good agreement with the experimental J_{SC}. A stabilized photocurrent density of 19.1 mA/cm for the **P65**-based PSC devices was determined by applying a constant bias voltage taken from the maximum power point at 0.90 V, as shown in Fig. 4(g), corresponding to a stabilized efficiency of 17.3%. These results demonstrate that a **P65**-based device exhibits a highly stable power output, as well as an extremely fast photo-response, thus further suggesting the reliability of the above device performance and indicating the efficient charge extraction and low charge recombination losses in **P65**-based devices. In addition, Fig. S10 summarizes the statistical data of **P65**-based cells from the synthesis of three individual batches, which demonstrates the good reproducibility of the materials and the solar cell devices.

There is no doubt that **P65**-based PSCs offer the best photovoltaic performance among the three HTMs under dopant-free conditions. We may also compare the champion dopant-free HTM-based PSCs under regular doping conditions, the results of which are shown in Fig. S11 and Table S4. It is not surprising that the monomeric **X65**-based PSC devices showed a similar photovoltaic performance as cells based on the standard Spiro-OMeTAD after doping because both molecular materials have similar intrinsic properties. This also illustrates that the monomeric material **X65** can be considered a replacement for traditional Spiro-OMeTAD when applied in devices and when dopants/additives are used. It is notable that the **P65**-based dopant-free PSC devices exhibit a comparable efficiency as compared to the other two types of devices based on doped HTMs. In addition, the estimated cost of **P65** used in solar cell devices is only 2.68% as

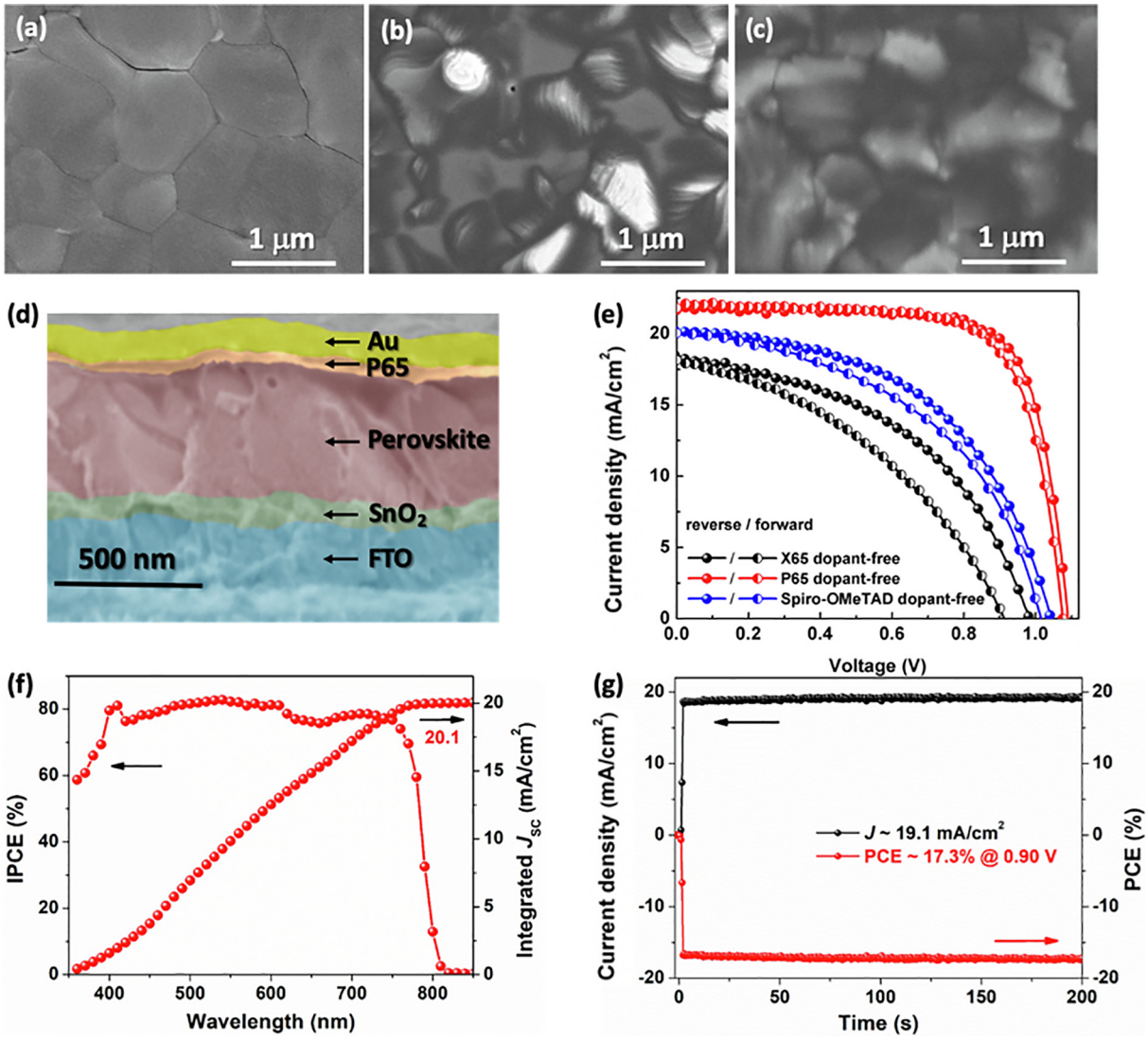

Fig. 4. Top view of perovskite films (a) without HTMs and with dopant-free HTM of (b) **X65** and (c) **P65**. (d) Cross-sectional SEM image of a device with **P65**, (e) *J–V* characteristics of dopant-free **X65**, **P65**, and Spiro-OMeTAD-based PSCs recorded under irradiation of 100 mW/cm^2 AM 1.5G light, (f) the corresponding IPCE spectra and integrated J_{SC} of dopant-free **P65**-based devices, and (g) steady-state output of photocurrent density and PCE of **P65**-based devices determined at the maximum power point when illuminated under 1 sun and AM 1.5G conditions.

Table 2
Photovoltaic parameters of the devices based on the dopant-free HTMs **X65**, **P65**, and Spiro-OMeTAD.

HTMs	Scan direction	J_{SC} (mA/cm^2)	V_{OC} (V)	FF (%)	η (%)
X65	Reverse	18.4	0.98	46.8	8.4
	Forward	18.1	0.91	39.7	6.5
P65	Reverse	21.7	1.09	75.0	17.7
	Forward	21.7	1.08	72.3	16.9
Spiro-OMeTAD	Reverse	20.1	1.04	51.0	10.6
	Forward	20.0	1.01	47.7	9.7

compared to the standard material Spiro-OMeTAD (Table S7), which is mainly due to the easy synthesis procedure of **P65** and the small amount of material required in such devices. This result indicates that **P65** has potential for large-scale industrial application in PSCs.

To further explore the charge recombination properties, electrochemical impedance spectroscopy (EIS) was conducted by applying a bias voltage of 0 V to 0.8 V under the illumination of simulated one sun light intensity. An equivalent circuit model was used to evaluate the EIS response, and the extracted charge recombination resistance (R_{rec}) at the interfaces is as shown in Fig. S13(a). Clearly, the R_{rec} of the **P65**-based device is higher than that of the other two HTM-based devices at different bias voltages. The larger R_{rec} value indicates a retarded charge recombination loss between interfaces, which is in good accordance with the higher J_{SC} and FF obtained by the **P65**-based devices. In addition, Fig. S13(b) shows the transient photovoltage decay in the PSCs under open-circuit conditions. In principle, a longer decay time implies a slower charge recombination [62]. Hence, the **P65**-based hole transport layer can more efficiently suppress the surface charge recombination in solar cell devices.

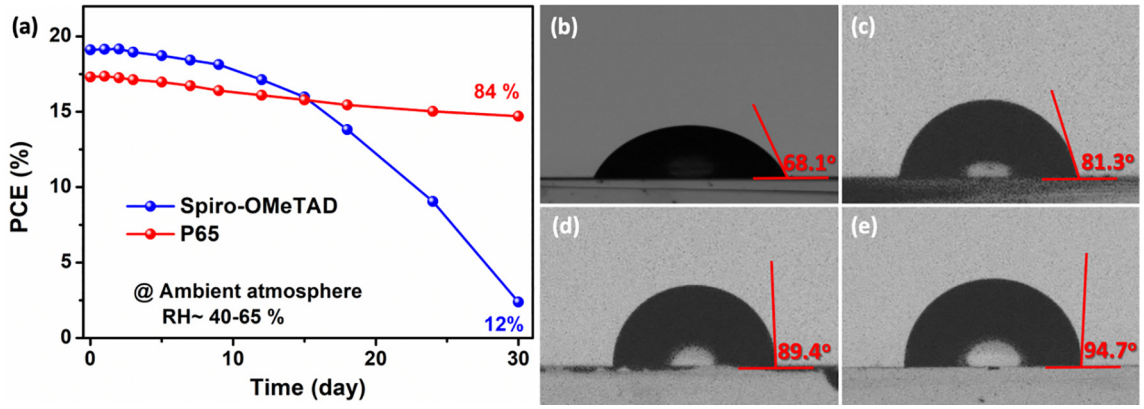

Fig. 5. (a) Stability of unsealed PSCs based on dopant-free **P65** and standard Spiro-OMetAD with dopants, recorded in an ambient atmosphere with a humidity of 40%–65% under 100 mW/cm^2 AM 1.5G illumination for 30 day, and contact angle measurements of water droplets on a perovskite layer covered by HTM layers of (b) doped Spiro-OMeTAD, (c) dopant-free Spiro-OMeTAD, (d) dopant-free **X65**, and (e) dopant-free **P65** samples, respectively.

The long-term stability of the unencapsulated devices was stored in an ambient atmosphere with a humidity of 40%–65% (Fig. 5a). After 30 day, the dopant-free **P65**-based PSC devices maintain 84% of the original PCE, whereas the doped Spiro-OMeTAD-based devices only retain 12% of the initial efficiency. The hydrophobicity of the hole transport layer is extremely important for the stability of a PSC because it can protect the perovskite layer against moisture. We further determined the hydrophobicity of **P65**, **X65**, and Spiro-OMeTAD layers through a contact angle measurement with water droplets, as shown in Fig. 5(b)–5(e). The **P65**-based hole transport layer exhibited the largest contact angle of close to 95° among all three materials, which indicates a good hydrophobic ability. This is also in good agreement with the device stability testing shown in Fig. 5(a). The much better stability of a dopant-free **P65**-based device can be attributed to its intrinsic hydrophobic property and the absence of hydrophilic additives. Consequently, a remarkable long-term stability along with a high PCE highlight the potential application of **P65** as an efficient dopant-free HTM for use in future PSCs.

4. Conclusions

We successfully designed and synthesized a novel crosslinked polymer **P65** through a mild free-radical polymerization with low-cost raw materials for application in conventional n-i-p type PSCs. The corresponding dopant-free PSCs based on **P65** exhibit a maximum efficiency of 17.7%, which transcend the standard Spiro-OMeTAD based devices (10.6%). The photo-electrochemical, opto-electronic, and thermal properties of the newly designed polymer were systematically investigated. Our study highlights the potential application of low-cost, polymeric, crosslinked, SFX-skeleton-based molecules as dopant-free HTMs for efficient and stable PSCs. This study also describes a new design strategy of SFX-based molecules and polymers for application in some other opto-electronic devices, such as OLEDs, perovskite-LEDs, and perovskite tandem solar cells. Future work will focus on the development of co-polymers by introducing another functionalized monomer into the **X65** to further control the opto-electronic properties of the materials.

Declaration of Competing Interest

The authors declare that they have no known competing financial interests or personal relationships that could have appeared to influence the work reported in this paper.

Acknowledgments

The authors are grateful for the support of the Swedish Energy Agency and Swedish Foundation for Strategic Research (SSF) for their financial support. Special acknowledgement is given to Dr. Fusheng Li for the assistance with the MALDI-TOF at Dalian University of Technology, China. L.H. and Y.G. would like to thank the National Supercomputer Centre at Linköping University for the computational resources. L.W., T.L., and W.Z. acknowledge the China Scholarship Council (CSC) for its financial support. J.G. gratefully acknowledges the support from the Swedish government through the research initiative "STandUP for ENERGY." Finally, L. W. and F.Z. contributed equally to this study.

Appendix A. Supplementary data

Supplementary data to this article can be found online at https://doi.org/10.1016/j.jechem.2020.06.062.

References

[1] M.M. Lee, J. Teuscher, T. Miyasaka, T.N. Murakami, H.J. Snaith, Science 338 (2012) 643.
[2] H.-S. Kim, C.-R. Lee, J.-H. Im, K.-B. Lee, T. Moehl, A. Marchioro, S.-J. Moon, R. Humphry-Baker, J.-H. Yum, J.E. Moser, M. Grätzel, N.-G. Park, Sci. Rep. 2 (2012) 591.
[3] A. Kojima, K. Teshima, Y. Shirai, T. Miyasaka, J. Am. Chem. Soc. 131 (2009) 6050–6051.
[4] L. Gao, F. Zhang, X. Chen, C. Xiao, B.W. Larson, S.P. Dunfield, J.J. Berry, K. Zhu, Angew. Chem. Int. Ed. 58 (2019) 11737–11741.
[5] R. Wang, J. Xue, L. Meng, J.-W. Lee, Z. Zhao, P. Sun, L. Cai, T. Huang, Z. Wang, Z.-K. Wang, Y. Duan, J.L. Yang, S. Tan, Y. Yuan, Y. Huang, Y. Yang, Joule 3 (2019) 1464–1477.
[6] Y. Yang, Z. Liu, W.K. Ng, L. Zhang, H. Zhang, X. Meng, Y. Bai, S. Xiao, T. Zhang, C. Hu, K.S. Wong, S. Yang, Adv. Funct. Mater. 29 (2019) 1806506.
[7] D. Xu, X. Hua, S.-C. Liu, H.-W. Qiao, H.-G. Yang, Y.-T. Long, H. Tian, Chem. Commun. 54 (2018) 5434–5437.
[8] P. O'Keeffe, D. Catone, A. Paladini, F. Toschi, S. Turchini, L. Avaldi, F. Martelli, A. Agresti, S. Pescetelli, A.E. Del Rio Castillo, F. Bonaccorso, A. Di Carlo, Nano Lett. 19 (2019) 684–691.
[9] L. Calio, S. Kazim, M. Gratzel, S. Ahmad, Angew. Chem. Int. Ed. Engl. 55 (2016) 14522–14545.
[10] O. Malinkiewicz, A. Yella, Y.H. Lee, G.M. Espallargas, M. Graetzel, M.K. Nazeeruddin, H.J. Bolink, Nat. Photonics 8 (2013) 128.
[11] E.H. Jung, N.J. Jeon, E.Y. Park, C.S. Moon, T.J. Shin, T.-Y. Yang, J.H. Noh, J. Seo, Nature 567 (2019) 511–515.
[12] Y. Hou, X. Du, S. Scheiner, D.P. McMeekin, Z. Wang, N. Li, M.S. Killian, H. Chen, M. Richter, I. Levchuk, N. Schrenker, E. Spiecker, T. Stubhan, N.A. Luechinger, A. Hirsch, P. Schmuki, H.-P. Steinrück, R.H. Fink, M. Halik, H.J. Snaith, C.J. Brabec, Science 358 (2017) 1192.
[13] M. Cheng, C. Chen, B. Xu, Y. Hua, F. Zhang, L. Kloo, L. Sun, J. Energy Chem. 24 (2015) 698–706.
[14] P. Liu, L. Wang, K.M. Karlsson, Y. Hao, J. Gao, B. Xu, G. Boschloo, L. Sun, L. Kloo, A.C.S. Appl, Mater. Interfaces 10 (2018) 35946–35952.

[15] S.H. Kang, C. Lu, H. Zhou, S. Choi, J. Kim, H.K. Kim, Dyes Pigm. 163 (2019) 734–739.
[16] X.-F. Zhang, C. Liu, J. Wu, B. Xu, J. Energy Chem. 43 (2020) 139–147.
[17] C. Lu, I.T. Choi, J. Kim, H.K. Kim, J. Mater. Chem. A 5 (2017) 20263–20276.
[18] W. Zhou, Z. Wen, P. Gao, Adv. Energy Mater. 8 (2018) 1702512.
[19] X. Jiang, D. Wang, Z. Yu, W. Ma, H.-B. Li, X. Yang, F. Liu, A. Hagfeldt, L. Sun, Adv. Energy Mater. 9 (2019) 1803287.
[20] L. Wang, J. Zhang, P. Liu, B. Xu, B. Zhang, H. Chen, A.K. Inge, Y. Li, H. Wang, Y.-B. Cheng, L. Kloo, L. Sun, Chem. Commun. 54 (2018) 9571–9574.
[21] K. Rakstys, C. Igci, M.K. Nazeeruddin, Chem. Sci. 10 (2019) 6748–6769.
[22] J. Zhang, B. Xu, L. Yang, A. Mingorance, C. Ruan, Y. Hua, L. Wang, N. Vlachopoulos, M. Lira-Cantú, G. Boschloo, A. Hagfeldt, L. Sun, E.M.J. Johansson, Adv. Energy Mater. 7 (2017) 1602736.
[23] X. Liu, E. Rezaee, H. Shan, J. Xu, Y. Zhang, Y. Feng, J. Dai, Z.-K. Chen, W. Huang, Z.-X. Xu, J. Mater. Chem. C 6 (2018) 4706–4713.
[24] A. Zheng, J. Wang, N. Xu, R. Zhu, Y. Yuan, J. Zhang, J. Zhang, Z. Li, P. Wang, ACS Photonics 5 (2018) 4694–4701.
[25] H.D. Pham, S.M. Jain, M. Li, S. Manzhos, K. Feron, S. Pitchaimuthu, Z. Liu, N. Motta, H. Wang, J.R. Durrant, P. Sonar, J. Mater. Chem. A 7 (2019) 5315–5323.
[26] J. Liu, Y. Wu, C. Qin, X. Yang, T. Yasuda, A. Islam, K. Zhang, W. Peng, W. Chen, L. Han, Energy Environ. Sci. 7 (2014) 2963–2967.
[27] C. Shen, Y. Wu, H. Zhang, E. Li, W. Zhang, X. Xu, W. Wu, H. Tian, W.-H. Zhu, Angew. Chem. Int. Ed. 58 (2019) 3784–3789.
[28] J. Zhou, X. Yin, Z. Dong, A. Ali, Z. Song, N. Shrestha, S.S. Bista, Q. Bao, R.J. Ellingson, Y. Yan, W. Tang, Angew. Chem. Int. Ed. 131 (2019) 13855–13859.
[29] C. Huang, W. Fu, C.Z. Li, Z. Zhang, W. Qiu, M. Shi, P. Heremans, A.K. Jen, H. Chen, J. Am. Chem. Soc. 138 (2016) 2528–2531.
[30] F. Zhang, X. Yang, M. Cheng, W. Wang, L. Sun, Nano Energy 20 (2016) 108–116.
[31] N. Arora, M.I. Dar, A. Hinderhofer, N. Pellet, F. Schreiber, S.M. Zakeeruddin, M. Gratzel, Science 358 (2017) 768–771.
[32] R. Chen, T. Bu, J. Li, W. Li, P. Zhou, X. Liu, Z. Ku, J. Zhong, Y. Peng, F. Huang, Y.-B. Cheng, Z. Fu, ChemSusChem 11 (2018) 1467–1473.
[33] R. Azmi, S.Y. Nam, S. Sinaga, Z.A. Akbar, C.-L. Lee, S.C. Yoon, I.H. Jung, S.-Y. Jang, Nano Energy 44 (2018) 191–198.
[34] J. Zhang, Q. Sun, Q. Chen, Y. Wang, Y. Zhou, B. Song, N. Yuan, J. Ding, Y. Li, Adv. Funct. Mater. 29 (2019) 1900484.
[35] F. Zhang, Z. Yao, Y. Guo, Y. Li, J. Bergstrand, C.J. Brett, B. Cai, A. Hajian, Y. Guo, X. Yang, J.M. Gardner, J. Widengren, S.V. Roth, L. Kloo, L. Sun, J. Am. Chem. Soc. 141 (2019) 19700–19707.
[36] J.H. Heo, S.H. Im, J.H. Noh, T.N. Mandal, C.-S. Lim, J.A. Chang, Y.H. Lee, H.-J. Kim, A. Sarkar, M.K. Nazeeruddin, M. Grätzel, S.I. Seok, Nat. Photonics 7 (2013) 486.
[37] P.J.S. Rana, R.K. Gunasekaran, S.H. Park, V. Tamilavan, S. Karuppanan, H.-J. Kim, K. Prabakar, J. Phys. Chem. C 123 (2019) 8560–8568.
[38] Y. Liu, Z. Hong, Q. Chen, H. Chen, W.-H. Chang, Y. Yang, T.-B. Song, Y. Yang, Adv. Mater. 28 (2016) 440–446.
[39] G.-W. Kim, G. Kang, J. Kim, G.-Y. Lee, H.I. Kim, L. Pyeon, J. Lee, T. Park, Energy Environ. Sci. 9 (2016) 2326–2333.
[40] S. Valero, S. Collavini, S.F. Völker, M. Saliba, W.R. Tress, S.M. Zakeeruddin, M. Grätzel, J.L. Delgado, Macromolecules 52 (2019) 2243–2254.
[41] S. Abraham, G.P.T. Ganesh, S. Varughese, B. Deb, J. Joseph, A.C.S. Appl, Mater. Interfaces 7 (2015) 25424–25433.
[42] E. Bellmann, S.E. Shaheen, S. Thayumanavan, S. Barlow, R.H. Grubbs, S.R. Marder, B. Kippelen, N. Peyghambarian, Chem. Mater. 10 (1998) 1668–1676.
[43] H.-L. Yip, A.K.Y. Jen, Energy Environ. Sci. 5 (2012) 5994–6011.
[44] J. Wu, C. Liu, B. Li, F. Gu, L. Zhang, M. Hu, X. Deng, Y. Qiao, Y. Mao, W. Tan, Y. Tian, B. Xu, A.C.S. Appl, Mater. Interfaces 11 (2019) 26928–26937.
[45] Y. Xu, T. Bu, M. Li, T. Qin, C. Yin, N. Wang, R. Li, J. Zhong, H. Li, Y. Peng, J. Wang, L. Xie, W. Huang, ChemSusChem 10 (2017) 2578–2584.
[46] B.R. Sutherland, Joule 2 (2018) 21–22.
[47] C.-E. Tsai, M.-H. Liao, Y.-L. Chen, S.-W. Cheng, Y.-Y. Lai, Y.-J. Cheng, C.-S. Hsu, J. Mater. Chem. C 3 (2015) 6158–6165.
[48] M.-H. Tremblay, K. Schutt, Y. Zhang, J. Lim, Y.-H. Lin, J.H. Warby, S. Barlow, H.J. Snaith, S.R. Marder, Sustain, Energy Fuels 4 (2020) 190–198.
[49] Y. Zhang, C. Kou, J. Zhang, Y. Liu, W. Li, Z. Bo, M. Shao, J. Mater. Chem. A 7 (2019) 5522–5529.
[50] J. Xu, O. Voznyy, R. Comin, X. Gong, G. Walters, M. Liu, P. Kanjanaboos, X. Lan, E.H. Sargent, Adv. Mater. 28 (2016) 2807–2815.
[51] J.C. Yu, J. Sun, N. Chandrasekaran, C.J. Dunn, A.S.R. Chesman, J.J. Jasieniak, Nano Energy 71 (2020) 104635.
[52] D. Bi, B. Xu, P. Gao, L. Sun, M. Grätzel, A. Hagfeldt, Nano Energy 23 (2016) 138–144.
[53] J. Zhang, Y. Hua, B. Xu, L. Yang, P. Liu, M.B. Johansson, N. Vlachopoulos, L. Kloo, G. Boschloo, E.M.J. Johansson, L. Sun, A. Hagfeldt, Adv. Energy Mater. 6 (2016) 1601062.
[54] K. Liu, Y. Yao, J. Wang, L. Zhu, M. Sun, B. Ren, L. Xie, Y. Luo, Q. Meng, X. Zhan, Mater. Chem. Front. 1 (2017) 100–110.
[55] B. Xu, J. Zhang, Y. Hua, P. Liu, L. Wang, C. Ruan, Y. Li, G. Boschloo, E.M.J. Johansson, L. Kloo, A. Hagfeldt, A.K.Y. Jen, L. Sun, Chem 2 (2017) 676–687.
[56] J. Wu, C. Liu, M. Hu, X. Deng, W. Tan, Y. Tian, B. Xu, J. Mater. Chem. A 6 (2018) 13123–13132.
[57] D. Moia, V. Vaissier, I. López-Duarte, T. Torres, M.K. Nazeeruddin, B.C. O'Regan, J. Nelson, P.R.F. Barnes, Chem. Sci. 5 (2014) 281–290.
[58] K.-H. Lin, A. Prlj, L. Yao, N. Drigo, H.-H. Cho, M.K. Nazeeruddin, K. Sivula, C. Corminboeuf, Chem. Mater. 31 (2019) 6605–6614.
[59] F.G. Zhang, J.Y. Cong, Y.Y. Li, J. Bergstrand, H.C. Liu, B. Cai, A. Hajian, Z.Y. Yao, L. Q. Wang, Y. Hao, X.C. Yang, J.M. Gardner, H. Agren, J. Widengren, L. Kloo, L.C. Sun, Nano Energy 53 (2018) 405–414.
[60] X. Jiang, J. Zhang, S. Ahmad, D. Tu, X. Liu, G. Jia, X. Guo, C. Li, Nano Energy 75 (2020) 104892.
[61] W. Yu, J. Zhang, D. Tu, Q. Yang, X. Wang, X. Liu, F. Cheng, Y. Qiao, G. Li, X. Guo, C. Li, Solar RRL 4 (2020) 1900367.
[62] Q. Jiang, Y. Zhao, X. Zhang, X. Yang, Y. Chen, Z. Chu, Q. Ye, X. Li, Z. Yin, J. You, Nat. Photonics 13 (2019) 460–466.